

A near-global climatology of oceanic coherent eddies

Josué Martínez-Moreno¹, Andrew McC. Hogg¹, and Matthew H. England²

¹Research School of Earth Science and ARC Center of Excellence for Climate Extremes, Australian National University, Canberra, Australia

²Climate Change Research Centre (CCRC), UNSW Australia, Sydney NSW, Australia

Key Points:

- Coherent eddies contain around 50% of the total surface ocean kinetic energy budget.
- Seasonal cycle of the number of coherent eddies and the coherent eddy amplitude reveals a 3-6 month lag to wind forcing.
- The seasonal lag between the number and the amplitude of coherent eddies suggests a role for the inverse cascade.

13 Abstract

14 Ocean eddies influence regional and global climate through mixing and transport of heat
15 and properties. One of the most recognizable and ubiquitous feature of oceanic eddies
16 are coherent vortices with spatial scales of tens to hundreds of kilometers, frequently re-
17 ferred as “mesoscale eddies”. Coherent mesoscale eddies are known to transport prop-
18 erties across the ocean and to locally affect near-surface wind, cloud properties and rain-
19 fall patterns. Although coherent eddies are ubiquitous, their climatology, seasonality and
20 long-term temporal evolution remains poorly understood. Here, we examine the kinetic
21 energy contained by coherent eddies and present the seasonal, interannual and long-term
22 variability using satellite observations between 1993 to 2019. A total of \sim 37 million co-
23 herent eddy are detected in this analysis. Around 50% of the kinetic energy contained
24 by ocean eddies corresponds to coherent eddies. Additionally, a strong seasonal cycle is
25 observed, with a 3–6 months lag between the wind forcing and the response of the co-
26 herent eddy field. The seasonality of the number of coherent eddies and their amplitude
27 reveals that the number of coherent eddies responds faster to the forcing (\sim 3 months),
28 than the coherent eddy amplitude (which lags by \sim 6 months). This seasonal cycle is spa-
29 tially variable, so we also analyze their climatology in key oceanic regions. Our analy-
30 sis highlights the relative importance of the coherent eddy field in the ocean kinetic en-
31 ergy budget, implies a strong response of the eddy number and eddy amplitude to forc-
32 ing at different time-scales, and showcases the seasonality, and multidecadal trends of
33 coherent eddy properties.

34 Plain language summary

35 Coherent eddies are the most common feature of ocean variability observable from
36 satellites. They are crucial in ocean dynamics as they can transport properties over long
37 distances and interact with the atmosphere. Our study investigates the seasonal, inter-
38 annual, and long-term changes in the abundance and intensity of coherent eddies, by au-
39 tomatically identifying individual eddies over the available satellite altimeter record. The
40 seasonal cycle suggests a transition from numerous, smaller, and weaker coherent eddies,
41 to fewer and larger, and stronger coherent eddies over the season. In addition, a long-
42 term adjustment of the coherent eddy field is identified with possible links to long-term
43 changes in the climate system.

44 1 Introduction

45 Mesoscale ocean variability with spatial scales of tens to hundreds of kilometers is
 46 comprised of processes such as vortices, waves, and jets (Ferrari & Wunsch, 2009; Fu et
 47 al., 2010). These mesoscale processes are highly energetic, and they play a crucial role
 48 in the transport of heat, salt, momentum, and other tracers through the ocean (Wun-
 49 sch & Ferrari, 2004; Wyrtki et al., 1976; Gill et al., 1974). One of the most recognizable
 50 and abundant ocean processes observable from space are mesoscale vortices. Although
 51 mesoscale vortices are commonly referred to in the literature as “mesoscale eddies”, this
 52 term is also often used to describe the total mesoscale ocean variability (the time-varying
 53 component of the mesoscale flow), thus, to avoid ambiguity we will refer to mesoscale
 54 vortices as *coherent eddies*. **Coherent eddies are abundant and energetic, but also**
 55 **essential to ocean dynamics as concluded by many previous studies** (Hogg &
 56 Blundell, 2006; Siegel et al., 2011; Beron-Vera et al., 2013; Frenger et al., 2013, 2015; Pilo
 57 et al., 2015; Schubert et al., 2019; Patel et al., 2020).

58 Coherent eddies are quasi-circular geostrophic currents. According to their rota-
 59 tional direction and the sign of the Coriolis parameter, the sea surface height anomaly
 60 within a coherent eddy can have a negative or positive sea surface height anomaly (cold-
 61 core and warm-core coherent eddies, respectively). This characteristic sea surface height
 62 signature of coherent eddies has been utilized to identify and track coherent eddies from
 63 satellite altimetry (e.g., Chelton et al., 2007; Faghmous et al., 2015; Ashkezari et al., 2016;
 64 Martínez-Moreno et al., 2019; Cui et al., 2020). Automated identification algorithms of
 65 coherent eddies have revealed their ubiquity in the oceans, with a predominant influence
 66 at hotspots of eddy activity such as in boundary current extensions and the Antarctic
 67 Circumpolar Current. In these regions, it has been estimated that coherent eddies con-
 68 tribute around 40–50% of the net mesoscale kinetic energy (Chelton et al., 2011) and thus
 69 a significant fraction of the total kinetic energy (Ferrari & Wunsch, 2009). Although this
 70 estimate showcases the importance of the mesoscale coherent eddy field, the energy con-
 71 tained by coherent eddies was estimated by extracting the total geostrophic velocity within
 72 the radius of each detected coherent eddy; thus, it is possible that this estimate may con-
 73 tain energy from other processes. Here we extend on this past work by reconstructing
 74 the surface imprint of coherent eddies using a new eddy tracking algorithm and using
 75 the latest available satellite record.

76 There is broad consensus that mesoscale eddy kinetic energy has a pronounced sea-
77 sonal variability (Qiu, 1999; Qiu & Chen, 2004; Kang & Curchitser, 2017; Uchida et al.,
78 2017). Several hypotheses have been proposed to explain this seasonality including: sea-
79 sonal variations of atmospheric forcing (Sasaki et al., 2014), seasonality of the mixed layer
80 depth (Qiu et al., 2014; Callies et al., 2015), seasonality of the intensity of barotropic in-
81 stability (Qiu & Chen, 2004), the variability of the baroclinic instability due to the sea-
82 sonality of the vertical shear (Qiu, 1999), and a seasonal lag of the inverse energy cas-
83 cade (i.e. energy is transported between scales, from small to large; Arbic et al., 2013)
84 in combination with the presence of a front in the mixed layer, which can lead to a sea-
85 sonal cycle of the baroclinic instability (Qiu et al., 2014). On one hand, processes such
86 as barotropic and baroclinic instabilities control the seasonality of coherent eddies in the
87 ocean. On the other hand, recent studies using observations and eddy-permitting climate
88 models suggest slower adjustments of the global ocean that create long-term changes in
89 the coherent eddy field. Such readjustments include a multidecadal increase in the ocean
90 stratification resulting from temperature and salinity changes (Li et al., 2020), a hori-
91 zontal readjustment of sea surface temperature gradients (Cane et al., 1997; Bouali et
92 al., 2017; Ruela et al., 2020), and an intensification of the kinetic energy, eddy kinetic
93 energy, and mesoscale eddy kinetic energy over the last 3 decades as a consequence of
94 an increase in wind forcing (Hu et al., 2020; Wunsch, 2020; Martínez-Moreno et al., 2021).
95 All of these seasonal factors and long-term readjustments directly influence the annual
96 and decadal response of the coherent eddy field, however, the seasonality of the coher-
97 ent component of the eddy kinetic energy, as well as the seasonal cycle and trends of the
98 coherent eddy statistics, remain unknown.

99 Here we present a new global climatology of the coherent eddy kinetic energy by
100 reconstructing the coherent eddy signature from satellite observations. Our study doc-
101 uments the seasonal cycle of the coherent eddy kinetic energy, and the seasonal cycle and
102 long-term trends of the coherent eddy properties over the satellite record. Moreover, we
103 conduct more detailed analyses in regions where coherent eddies dominate the eddy ki-
104 netic energy field. The rest of this paper is structured as follows: the data sources and
105 methodology are described in Section 2. Then, we present the climatology, energy ra-
106 tios, and global seasonality of the coherent eddy kinetic energy in Section 3. Section 4
107 outlines the global climatology and seasonality of coherent eddy properties, followed by
108 long-term changes of the coherent eddy properties (Section 5). Then we focus our at-

109 tention on the seasonal cycle and coherent eddy properties in regions dominated by co-
 110 herent eddies (Section 6). Finally, Section 7 summarizes the main results and discusses
 111 the implications of this study.

112 **2 Methods**

113 We use daily sea surface height (SSH) data made available by the Copernicus Ma-
 114 rine Environment Monitoring Service in near real time (CMEMS, 2017). This gridded
 115 product contains the sea surface height and geostrophic velocities with daily 0.25° res-
 116 olution from January 1993 to 2019. The daily geostrophic velocities allow us to compute
 117 the kinetic energy (KE) and eddy kinetic energy (EKE) over the satellite record. The
 118 main source of EKE is the time-varying wind (Ferrari & Wunsch, 2009); thus, we also
 119 compute the seasonal cycle of the wind magnitude from the JRA55 reanalysis (Japan
 120 Meteorological Agency, Japan, 2013) using wind velocities at 10m above the ocean's sur-
 121 face.

122 Over the same record, coherent eddy statistics from Martínez-Moreno et al. (2019),
 123 hereafter MM19, are analyzed and compared with those released by Chelton & Schlax
 124 (2013), hereafter CS13. Both datasets are gridded in a 1° resolution and are produced
 125 via automated eddy identification algorithms using closed contours of SSH. However, these
 126 datasets have important differences in the criteria they use to identify and record coher-
 127 ent eddies statistics. The major differences include: (i) MM19's algorithm requires an
 128 adjustment between a 2D Gaussian and the SSH anomaly (SSHa) surface within the iden-
 129 tified closed contour, while CS13's only uses the outermost closed contour of SSH; (ii)
 130 MM19's dataset reports the maximum SSHa within the identified coherent eddy, while
 131 CS13's algorithm reports the maximum SSH value minus the discrete level in which the
 132 coherent eddy was identified; and (iii) MM19's dataset includes all detected coherent ed-
 133 dies, while CS13's dataset excludes coherent eddies with lifetimes shorter than four weeks
 134 and coherent eddy amplitudes smaller than 1cm. Moreover, MM19's algorithm allows
 135 the reconstruction of the coherent eddy field under the assumption that coherent eddies
 136 have a 2D Gaussian imprint in the sea surface height. This Gaussian reconstruction of
 137 the coherent eddy field then allows us to estimate the coherent geostrophic eddy veloc-
 138 ities and thus the kinetic energy contained only by coherent eddies.

139 **2.1 Kinetic Energy decomposition**

140 Kinetic energy is commonly divided into the mean and time-varying components
 141 through a Reynolds decomposition. At a given time, the surface velocity field $\mathbf{u} = (u, v)$
 142 is split into the time mean ($\bar{\mathbf{u}}$) and time varying components (\mathbf{u}'). Moreover, MM19 pro-
 143 posed to further decompose the eddy kinetic energy into the energy contained by coher-
 144 ent features (\mathbf{u}'_e) and non-coherent features (\mathbf{u}'_n). Therefore the KE equation can be writ-
 145 ten as:

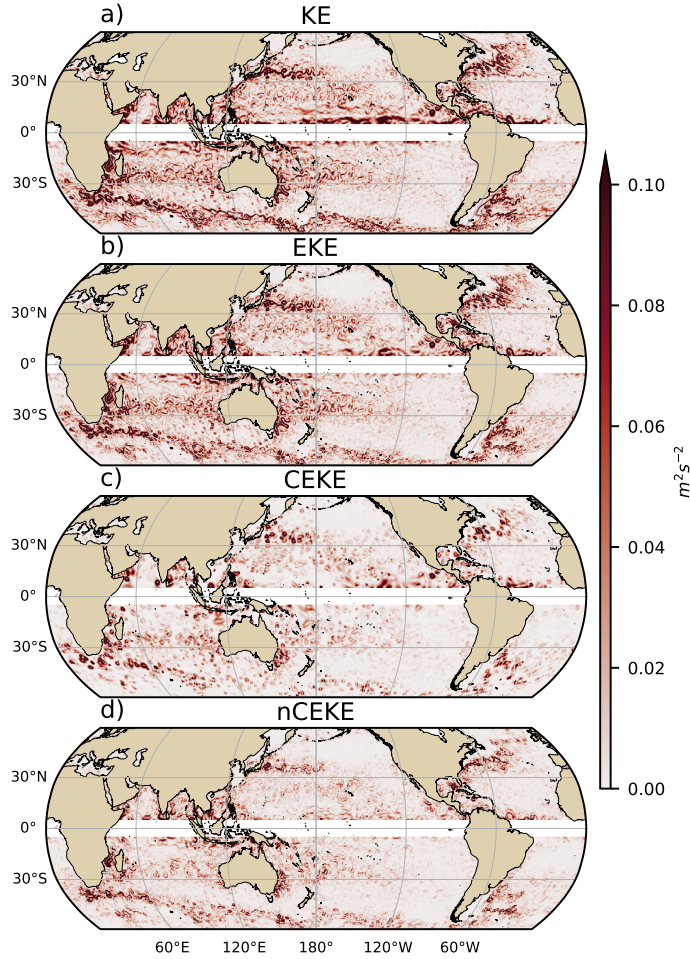
$$\text{KE} = \underbrace{\bar{u}^2 + \bar{v}^2}_{\text{MKE}} + \underbrace{u'^2_e + v'^2_e}_{\text{CEKE}} + \underbrace{u'^2_n + v'^2_n}_{\text{nCEKE}} + \mathcal{O}_c^2 + \mathcal{O}^2 \quad (1)$$

146 Due to the properties of this decomposition, the second order term \mathcal{O}^2 is zero when
 147 averaged over the same period as $\bar{\mathbf{u}}$. However, \mathcal{O}_c^2 is not necessarily negligible, unless it
 148 is averaged over time and space. More information about the decomposition of the field
 149 into coherent features and non-coherent features is explained in Martínez-Moreno et al.
 150 (2019). A global snapshot of each component of kinetic energy decomposition is shown
 151 in Figure 1, where the KE and EKE are comprised of rings and filaments. As expected,
 152 the decomposition of EKE into CEKE and nCEKE components exhibits only the ring-
 153 like signatures expected of coherent eddies, while the non-coherent component primar-
 154 ily shows filaments, with some mis-identified coherent eddies.

158 **2.2 Eddy statistics**

159 The eddy statistics used in this study include (i) the eddy count ($cEddy_n$) defined
 160 as the number of coherent eddies per grid cell, (ii) the eddy diameter defined as the di-
 161 ameter of a circle with equal area to the closed contour of each identified eddy, and (iii)
 162 the mean eddy amplitude defined as the mean amplitude of the coherent eddies within
 163 the cell ($cEddy_{amp}$). The latter metric can be separated into positive ($cEddy_{amp}^+$) and
 164 negative ($cEddy_{amp}^-$) coherent eddy amplitudes, defined as the mean amplitude of warm
 165 core and cold core coherent eddies, respectively, within the cell. The polarity indepen-
 166 dent eddy amplitude ($|cEddy_{amp}|$) is defined as:

$$|cEddy_{amp}| = \frac{1}{2} (cEddy_{amp}^+ - cEddy_{amp}^-) \quad (2)$$



155 **Figure 1.** Snapshot of surface kinetic energy (\overline{KE}), surface eddy kinetic energy (\overline{EKE}),
 156 surface coherent eddy kinetic energy (\overline{CEKE}), and surface non-coherent eddy kinetic energy
 157 (\overline{nCEKE}) for the 1st of January 2017.

167 Note that the $cEddy_{amp}^+$ and $cEddy_{amp}^-$ are sign definite, thus the difference will always
 168 be positive, whereas the gridded averaged $cEddy_{amp}$ can be negative or positive noting
 169 the dominant polarity of coherent eddies in the region, and the absolute value of $cEddy_{amp}$
 170 is denoted by $cEddy_{|amp|}$. We analyze the climatology and trends of the above eddy statis-
 171 tics over the available satellite record, namely between 1993 and 2019. We exclude the
 172 equatorial region ($10^\circ S - 10^\circ N$) and regions poleward of 60° , because the geostrophic ap-
 173 proximation is invalid near the Equator and the satellite spatial coverage at high-latitudes
 174 is unable to resolve the coherent eddy scales polewards of 60° . Note that the climatol-
 175 ogy of $cEddy_n$ is computed by adding all the identified eddies over the record, while all

other climatological statistics are computed as the time-average over the record. Seasonal climatologies are calculated for the monthly average of each coherent eddy statistic, while hemispheric time-series are filtered with a running average of 90 days. Trends of $cEddy_n$ and $|cEddy_{amp}|$ are calculated by coarsening the dataset to a 5° grid, and then linear trends are computed for each grid point. The statistical significance of trends is assessed by a modified Mann-Kendall test above the 95% confidence level (Yue & Wang, 2004).

Time averages are denoted by $\overline{}$, while area-weighted averages are denoted using $\langle \rangle$, where the area-weighted average of a function f is:

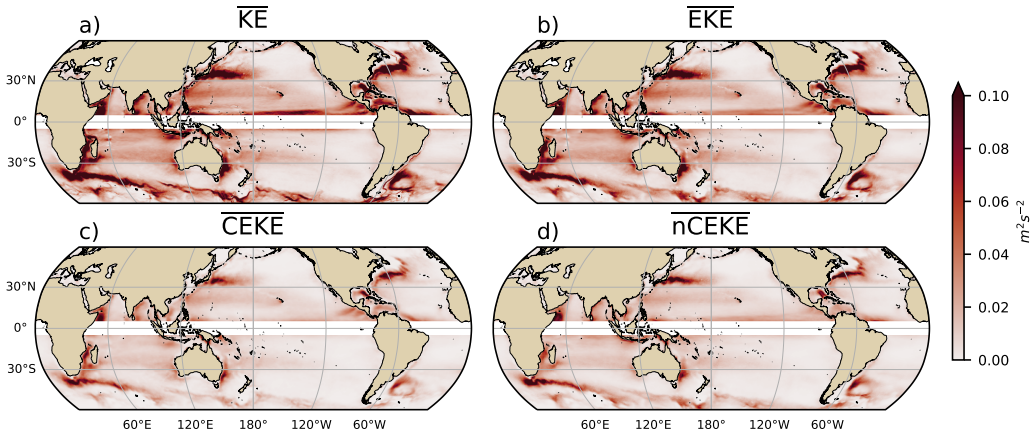
$$\langle f \rangle = \frac{\int f \xi dx dy}{\int \xi dx dy}, \quad (3)$$

where ξ is a mask that is set to zero in grid cells where no coherent eddies were identified and one elsewhere.

3 Global Coherent Eddy Energetics

The kinetic energy decomposition estimated from sea surface height measured by satellite altimeters averaged from 1993-2019 is shown in Figure 2. These maps show that many regions of the global ocean are highly energetic in mean KE (\overline{KE}), mean EKE (\overline{EKE}), mean coherent eddy kinetic energy (\overline{CEKE}) and mean non-coherent eddy kinetic energy (\overline{nCEKE}). The spatial pattern highlights well-known regions of the ocean where mesoscale processes are abundant, such as the western boundary current (WBC) extensions and the Antarctic Circumpolar Current. The spatial distribution of the energy contained by the reconstructed mesoscale coherent eddies and non-coherent components are similar (Figures 2c,d). However, there are some regions where coherent eddies dominate over non-coherent, and vice-versa. Overall, this decomposition suggests that boundary current extensions and other energetic regions of the ocean contain both coherent and non-coherent components of the kinetic energy.

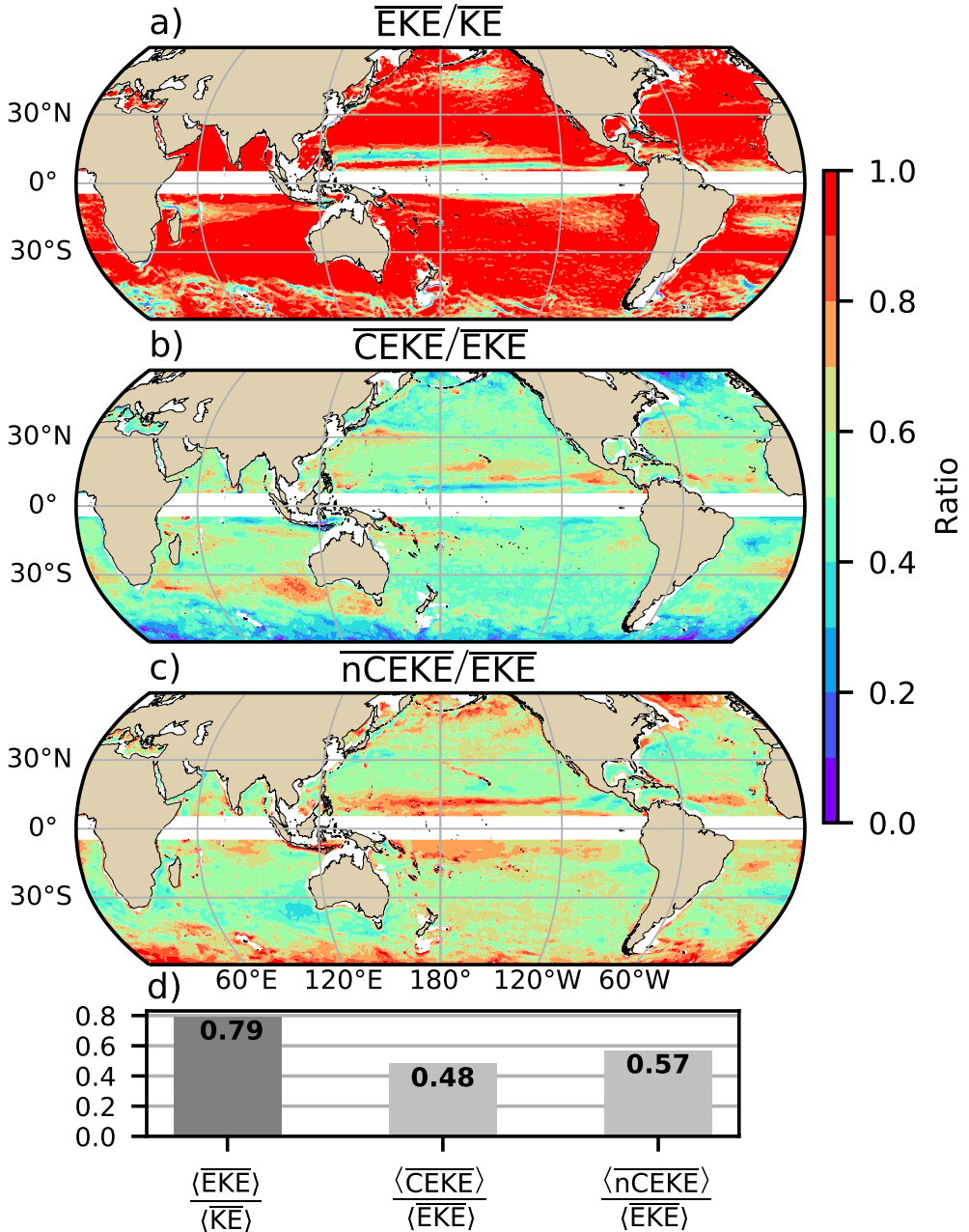
Eddy kinetic energy is known to be more than an order of magnitude greater than kinetic energy of the mean flow (MKE; Gill et al., 1974); this result is clearly shown in Figure 3a, which indicates that \overline{EKE} is responsible for almost all the \overline{KE} across the ocean, except for regions with persistent currents over time. Such regions are located in the mean boundary extension locations, the equatorial Pacific currents and regions in the Antarctic Circumpolar Current, where the \overline{EKE} explains around 40% of the \overline{KE} . In a previ-



200 **Figure 2.** a) Mean surface kinetic energy (\overline{KE}); b) surface eddy kinetic energy (\overline{EKE}); c)
201 surface coherent eddy kinetic energy (\overline{CEKE}), and d) surface non-coherent eddy kinetic energy
202 (\overline{nCEKE}) averaged between 1993-2018.

218 ous study, Chelton et al. (2011) estimated that the EKE within coherent eddies with life-
219 times greater than 4 weeks contain between 40-60% of the \overline{EKE} . Our method to recon-
220 struct the coherent eddy signature (Figure 3b) further corroborates that the coherent
221 eddy component ($\langle \overline{CEKE} \rangle$) has ~48% of the $\langle \overline{KE} \rangle$ (Figure 3d). Furthermore, global area
222 averages of the ratios show that $\langle \overline{EKE} \rangle$ explains ~78% of the ocean $\langle \overline{KE} \rangle$ field, while
223 non coherent eddy features contain ~57% percent of the $\langle \overline{EKE} \rangle$. Note that the globally
224 averaged coherent and non coherent components do not add to 100% as the cross terms
225 (O_c^2) are **non-zero (up to -10%)**. The spatial pattern reveals a dominance of the \overline{CEKE}
226 equatorward from the boundary current extensions and in areas with large coherent eddy
227 contributions of around 80% of the region's eddy kinetic energy, such as south of Aus-
228 tralia, in the Tehuantepec Gulf, and in the tropical Atlantic. An evident signal is a re-
229 duction of the energy contained by coherent eddies at high latitudes and an increase in
230 the energy explained by non-coherent eddies; this signal could be a consequence of the
231 inability of the 0.25° satellite resolution (~ 13 km at 60° latitude) to resolve coherent
232 eddies with scales smaller than ~ 10 km (first baroclinic Rossby radius at 60° ; Chelton
233 et al., 1998).

234 Figure 4 shows the seasonal cycle of the area-weighted EKE and CEKE for the North-
235 ern Hemisphere ($\langle EKE \rangle_{NH}$ and $\langle CEKE \rangle_{NH}$; $10^\circ N - 60^\circ N$) and Southern Hemisphere
236 ($\langle EKE \rangle_{SH}$ and $\langle CEKE \rangle_{SH}$; $60^\circ S - 10^\circ S$). In both hemispheres, the $\langle EKE \rangle$ and $\langle CEKE \rangle$



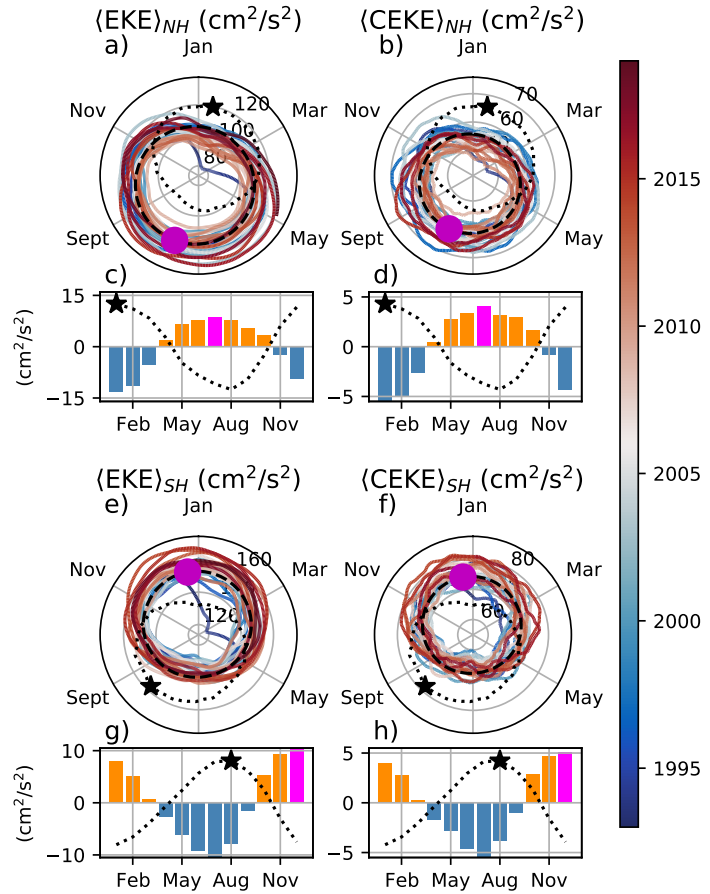
203 **Figure 3.** Ratios of the kinetic energy components. a) Map of the proportion of mean eddy
 204 kinetic energy (\overline{EKE}) versus mean kinetic energy (\overline{KE}); b) Map of the fraction of mean coherent
 205 eddy kinetic energy (\overline{CEKE}) versus mean eddy kinetic energy (\overline{EKE}); c) Map of the fraction of
 206 mean non-coherent eddy kinetic energy (\overline{nCEKE}) versus mean eddy kinetic energy (\overline{EKE}); d)
 207 Global time and area averaged (represented by $\langle \rangle$) fraction of mean eddy kinetic energy ($\langle \overline{EKE} \rangle$)
 208 versus the global mean kinetic energy ($\langle \overline{KE} \rangle$), area averaged fraction of mean coherent eddy
 209 kinetic energy ($\langle \overline{CEKE} \rangle$) and mean non coherent eddy kinetic energy ($\langle \overline{nCEKE} \rangle$) versus global
 210 mean eddy kinetic energy ($\langle \overline{EKE} \rangle$). Regions where the depth of the ocean is shallower than
 211 1000m are removed from the ratio estimation.

peak during summer. In the Northern Hemisphere, the largest $\langle \text{EKE} \rangle_{NH}$ and $\langle \text{CEKE} \rangle_{NH}$ occurs in July, ~ 6 months after the maximum winds in January (purple bar and black star in Figure 4c and d). Meanwhile, the Southern Ocean $\langle \text{EKE} \rangle_{SH}$ and $\langle \text{CEKE} \rangle_{SH}$ seasonal maxima arises during December, ~ 4 months after the maximum winds in August (purple bar and back star in Figure 4g, and h). This lag between winds and the eddy and coherent eddy energy components is further discussed in Section 4.

The cyclic plots in Figure 4 show the temporal evolution of $\langle \text{EKE} \rangle$ and $\langle \text{CEKE} \rangle$. Note that high frequency variability can be observed in the $\langle \text{CEKE} \rangle$ field with temporal scales of a few months, this variability could be attributed to regional dynamics averaged over the hemisphere (boundary currents, ocean gyres, etc.), as well as errors within the coherent eddy reconstruction. Additionally, concentric changes in the cyclic plots highlight long-term changes over the record. For example, the Northern Hemisphere winters during early years of the record (blue) had a more energetic coherent eddy field, which has transitioned to weaker coherent energy content since 2010 (red), in other words, the intensity of the $\langle \text{CEKE} \rangle_{NH}$ field has decreased. A larger long-term change can be observed in the Southern Hemisphere, where concentric growth over time in $\langle \text{EKE} \rangle_{SH}$ and $\langle \text{CEKE} \rangle_{SH}$ supports the previously observed strengthening of the eddy field in the Southern Ocean (Hogg et al., 2015; Martínez-Moreno et al., 2019; Martínez-Moreno et al., 2021).

4 Global Coherent Eddy Statistics

Coherent eddy kinetic energy allows us to quantify and study the energy of the eddy field, but the coherent eddy properties computed by automated coherent eddy identification algorithms allow us to further investigate the contribution and temporal changes of their abundance (i.e. the number of eddies) and their intensity (both their amplitude and diameter). Figure 5 shows gridded estimates of the number of eddies and the eddy amplitude. In this analysis, we contrast our MM19 eddy count with that of CS13 (Chelton et al., 2007; Figure 5a-b). Although the number of identified eddies is larger in MM19, possibly due to the lifespan filter implemented by CS13, both datasets reveal consistent spatial patterns. For example, both datasets show an important meridional variation in the abundance of eddies, with high numbers of eddies in mid-latitudes and fewer eddies in the tropics and at high-latitudes ($\sim 60^\circ$). Additionally, there is a tendency at mid-latitudes (30°) for higher numbers of eddies in the eastern side of ocean basins (e.g. the East North Pacific, East North Atlantic, East South Pacific, and East South Atlantic). Another in-



255 **Figure 4.** Seasonality of the area-weighted eddy kinetic energy ($\langle EKE \rangle$) and coherent eddy
 256 kinetic energy ($\langle CEKE \rangle$). Panels a) and b) show the time-series of the Northern Hemisphere,
 257 while panels e) and f) correspond to the Southern Hemisphere. Panels c) and d) show the sea-
 258 sonal cycle of the $\langle EKE \rangle_{NH}$ and $\langle CEKE \rangle_{NH}$ in the Northern Hemisphere, and panels g) and h)
 259 show the Southern Hemisphere ($\langle EKE \rangle_{SH}$ and $\langle CEKE \rangle_{SH}$). Dashed lines correspond to the sea-
 260 sonal cycle of the fields and dotted lines show the seasonal cycle of the wind magnitude smoothed
 261 over 120 days (moving average). The black stars and magenta markers (circle and bar) show
 262 the maximum of the seasonal cycle for the kinetic energy components and the wind magnitude,
 263 respectively. In the cyclic plots, line colors shows the year.

teresting pattern emerges in both eddy count datasets, where small scale structures appear in the eddy count field. These small structures highlight preferred coherent eddy paths observable in boundary current extensions and over regions of the Southern Ocean. These structures and paths of coherent eddies could be associated with topographic features, with overall consistency between the eddy count patterns using the two different eddy identification methods.

Regions with large counts of eddies have, in general, **small absolute amplitudes (Figure 5c), for example, the eastern side of ocean basins.** The ocean gyre interiors have a larger absolute amplitude and finally regions such as the boundary current extensions and the Antarctic Circumpolar Current have the largest coherent eddy absolute amplitudes, as also shown by Chelton et al. (2011). Eddy amplitude highlights regions dominated by a given coherent eddy polarity, for example, boundary extensions have a preferred sign (Figure 5 d); namely, positive amplitude polewards of the boundary current extension mean location, and negative amplitude equatorwards. This sign preference is consistent with the preferential way that coherent eddies are shed from boundary current extensions; with warm core eddies (positive) polewards of the boundary current extension, and equatorward for cold core eddies (negative) (Chelton et al., 2007, 2011; Kang & Curchitser, 2013). These global statistics reveal the absolute coherent eddy amplitude as a proxy for the CEKE with similar spatial patterns (Figure 2 & Figure 5c) and showcases that in regions where $\overline{\text{CEKE}}$ has a large proportion of $\overline{\text{EKE}}$ (Figure 3), the absolute coherent eddy amplitude is also large.

To further understand the seasonal cycle of $\langle \text{CEKE} \rangle$, we compute the climatology of coherent eddy properties in each hemisphere (Figure 6). The seasonality of the number of eddies in the Northern Hemisphere peaks in April (Figure 6a, c), while the Southern Hemisphere maximum number of eddies occurs during October (Figure 6e, g). Meanwhile, the seasonality of the eddy amplitude ($\langle |c\text{Eddy}_{amp}| \rangle$) peaks in August and January for the Northern and Southern Hemispheres respectively (Figure 6b, d, f, and h). As expected, the seasonality of $\langle |c\text{Eddy}_{amp}| \rangle$, equivalent to the intensity of the coherent eddies, is consistent with the seasonal cycle of $\langle \text{CEKE} \rangle$.

A key feature of Figure 6 is a distinct lag of ~ 3 months between the winds and eddy count, while the eddy amplitude maximum occurs ~ 6 months after the seasonal maxima in winds. We suggest that the eddy number increases earlier in the year and, through

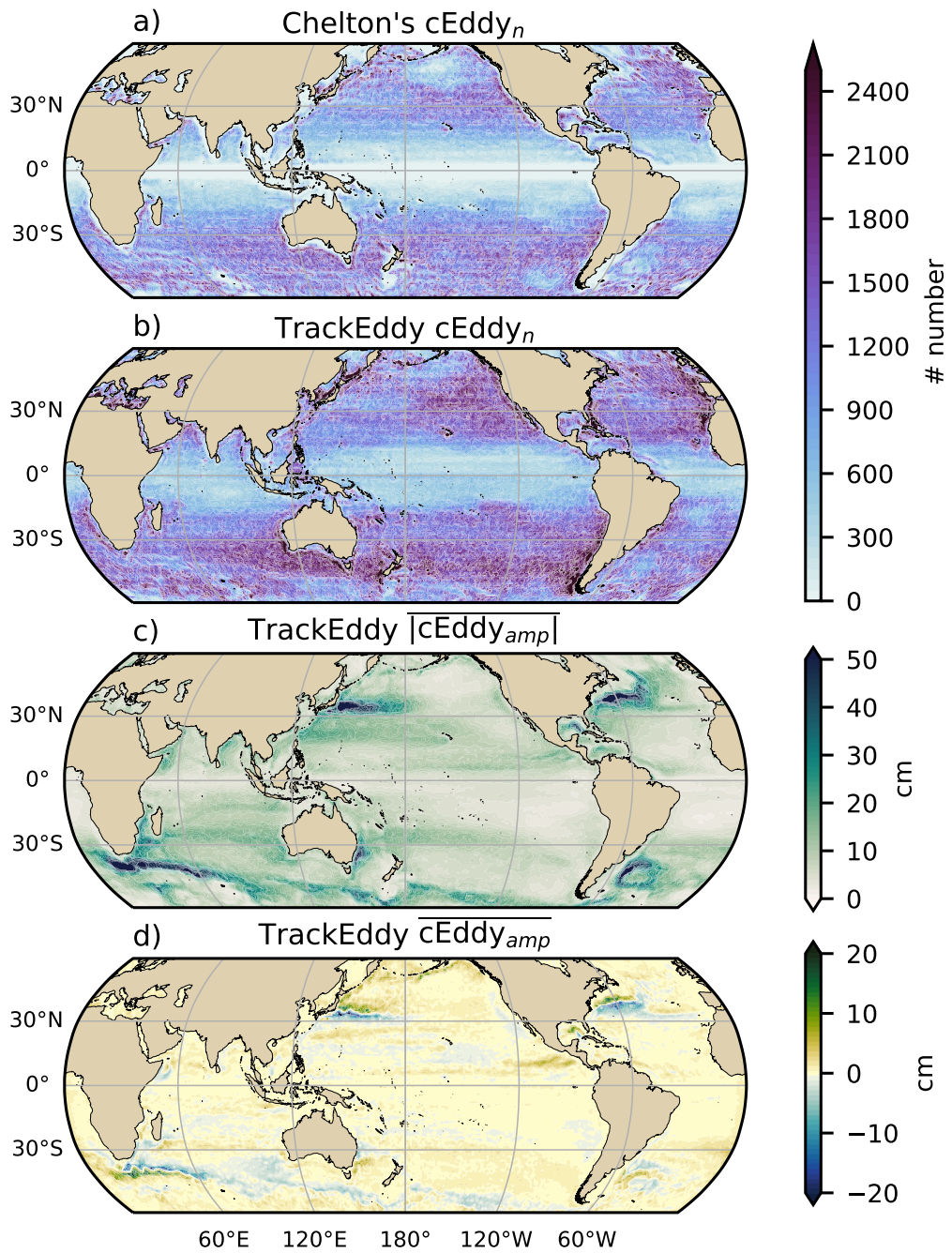
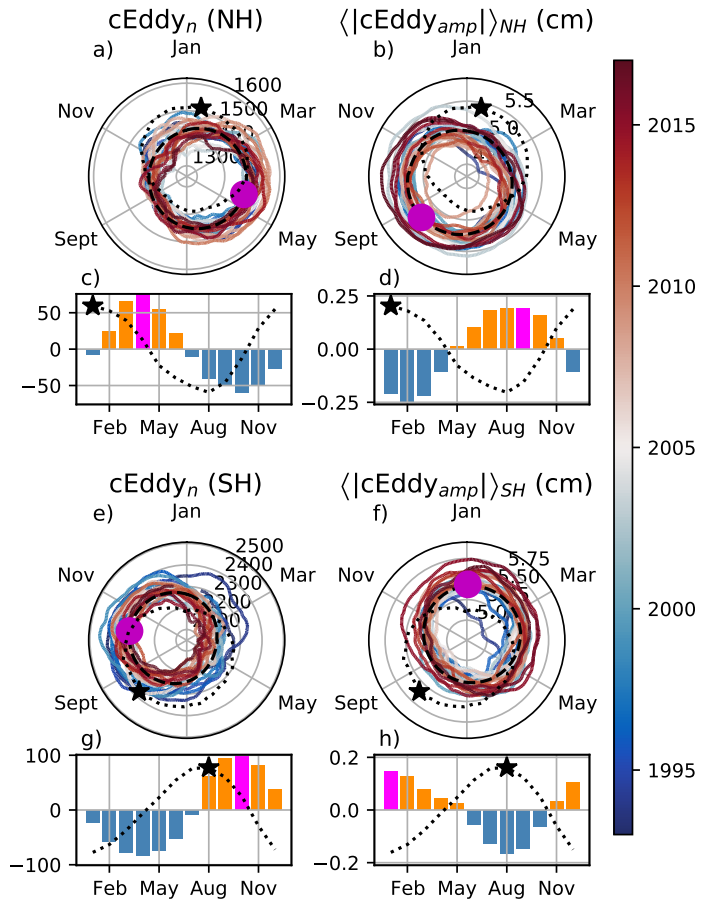


Figure 5. Averaged coherent eddy statistics. a) Climatology of the number of coherent eddies ($cEddy_n$) identified by Chelton et al. (2007); b) Climatology of the number of coherent eddies ($cEddy_n$) identified by Martínez-Moreno et al. (2019); c) Climatology of the mean absolute coherent eddy amplitude ($cEddy_{amp}$), and d) Climatology of the mean coherent eddy amplitude ($cEddy_{amp}$).

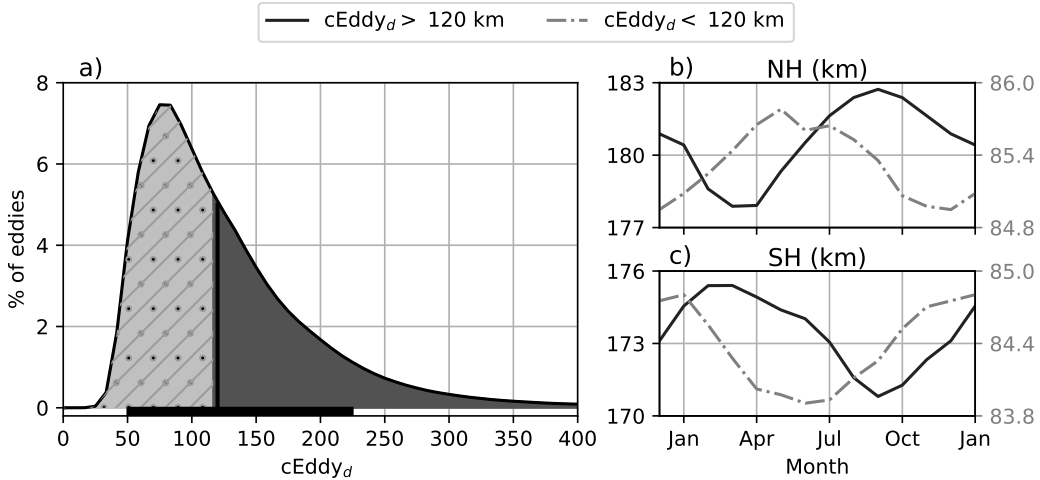
315 eddy-eddy interactions (merging of coherent eddies), the coherent eddy amplitude in-
 316 creases ~ 3 months after. This seasonal lag and summer maxima is consistent with pre-
 317 vious studies which suggest that a time-lag of the inverse cascade (Sasaki et al., 2014;
 318 Qiu et al., 2014) is responsible for the EKE seasonal cycle, where winter has the high-
 319 est energy at the smallest scales (non-resolvable with satellite observations), spring and
 320 autumn have the highest and lowest energy at scales of 50-100 km, and summertime has
 321 the highest energy at the largest scales (> 100 km; Uchida et al., 2017). Thus, the max-
 322 imum of $\langle \text{EKE} \rangle$, $\langle \text{CEKE} \rangle$, and $\langle |c\text{Eddy}_{amp}| \rangle$ located during summertime suggests that
 323 the seasonality of eddies and coherent eddies could be dominated by scales larger than
 324 100 km.

325 This result can be further explored by looking at the seasonal evolution of the eddy
 326 diameter ($c\text{Eddy}_d$). Note that 90% of identified coherent eddies have diameters between
 327 50 to 220 km (Figure 7a). We partition eddies into large-scale coherent eddies (diam-
 328 eter > 120 km) and small-scale coherent eddies (diameter < 120 km; Figure 7a). In the
 329 Northern Hemisphere, small-scale eddies have a seasonal peak in diameter during May,
 330 while large-scale eddies have the greatest diameter in September (Figure 7b). Meanwhile,
 331 in the Southern Hemisphere, the small-scale coherent eddies exhibit maximum dia-
 332 meter in December, while the diameter of large-scale coherent eddies peaks in February (Fig-
 333 ure 7 c). This result suggests that wind driven baroclinic instabilities generate small co-
 334 herent eddies early in the season, which then merge and grow to become larger in diam-
 335 eter and amplitude, and thus, more energetic. This process is likely associated with the
 336 inverse energy cascade, and suggests that this mechanism not only drives EKE season-
 337 ality, but also may be responsible for the seasonal cycle of coherent eddies.

353 Long-term changes can be observed in Figure 6a,b, e, and f where growing/shrinking
 354 concentric circles over time denote an increase/decrease trend of the field. This trend
 355 is particularly evident in the Southern Hemisphere, where the number of eddies has de-
 356 creased, while the eddy amplitude has increased. This result is consistent with the ob-
 357 served trends in EKE and mesoscale EKE in the Southern Ocean (Hogg et al., 2015; Martínez-
 358 Moreno et al., 2019). The coherent eddy amplitude from positive coherent eddies and
 359 negative coherent eddies show similar seasonal cycles to the absolute eddy amplitude.
 360 The Northern Hemisphere decrease in absolute eddy amplitude is driven by a decrease
 361 of the amplitude of negative coherent eddies in the Northern Hemisphere. Meanwhile



338 **Figure 6.** Seasonality of the count of number of eddies ($c\text{Eddy}_n$) and the area-weighted polar-
 339 erty independent coherent eddy amplitude ($\langle |c\text{Eddy}_{amp}| \rangle$); Panels a and b show the time-series of
 340 the Northern Hemisphere, while panels e and f correspond to the Southern Hemisphere. Panels
 341 c and d show the seasonal cycle of $c\text{Eddy}_n$ and $\langle |c\text{Eddy}_{amp}| \rangle_{NH}$ in the Northern Hemisphere,
 342 and panels g and h show the Southern Hemisphere, $c\text{Eddy}_n$ and $\langle |c\text{Eddy}_{amp}| \rangle_{SH}$. Dashed lines
 343 correspond to the seasonal cycle of the fields and dotted lines show the seasonal cycle of the wind
 344 magnitude, smoothed over 120 days (moving average). The black stars and magenta markers
 345 (circle and bar) indicate the maximum of the seasonal cycle for the eddy property, and the wind
 346 magnitude, respectively. In the cyclic plots, line colors show the year from 1993-2019.

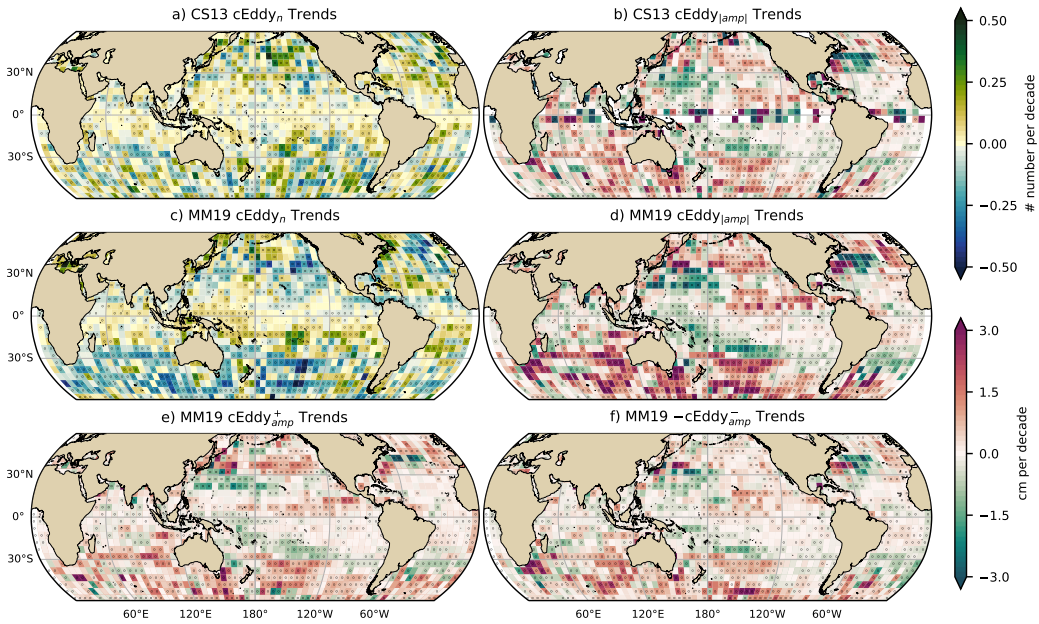


347 **Figure 7.** Distribution of the identified eddy diameter ($cEddy_d$; km) and hemispherical
 348 seasonality of the coherent eddy diameter. a) Distribution in percentage of identified eddy am-
 349 plitude, solid bar below distribution represents 90% of the identified eddies. Seasonal cycle of
 350 the eddy diameter for the b) Northern Hemisphere and c) Southern Hemisphere. Dark solid line
 351 and area corresponds to coherent eddies with diameters larger than 120 km, while light gray
 352 dash-dotted line and area shows coherent eddies with diameters smaller than 120 km.

362 in the Southern Ocean, the increase in absolute eddy amplitude is corroborated by a strength-
 363 ening of both coherent eddy polarities since the early 90s.

364 5 Trends

365 The results presented in Figures 4 and 6 suggest a long-term readjustment of the
 366 coherent eddy field. The long-term trends of the number of coherent eddies, absolute co-
 367 herent eddy amplitude, and coherent eddy amplitude polarities are further explored in
 368 Figure 8 contrasting the MM19 and CS13 methods. **Both MM19 and CS13 datasets**
 369 show consistent spatial patterns in the trends and significance of the number of coher-
 370 ent eddies and the absolute coherent eddy amplitude. Several regions in the ocean, such
 371 as the Southern Ocean, North Atlantic and North Pacific, show a decrease in the num-
 372 ber of eddies. Those same regions also have a clear increase in the absolute coherent eddy
 373 amplitude. These trends are similar to those observed in mesoscale eddy kinetic energy
 374 (Martínez-Moreno et al., 2021) and provide additional evidence of a readjustment of the
 375 mesoscale eddy field over the last 3 decades.



386 **Figure 8.** Trends of coherent eddy statistics. a) and b) Trends of the number of identified
 387 coherent eddies from satellite observations identified using the TrackEddy scheme of MM19,
 388 and those reported in CS13's dataset. c) and d) Trends of the absolute value of identified coher-
 389 ent eddy amplitude ($cEddy_{amp}$) from satellite observations identified using TrackEddy (after
 390 MM19), and those reported by CS13. e) and f) Trends of the eddy amplitude polarity using
 391 TrackEddy ($cEddy_{amp}^+$ and $cEddy_{amp}^-$). Gray stippling shows regions that are statistically signifi-
 392 cant above the 95% confidence level.

376 The observed trends of $cEddy_{amp}$ in several oceanic regions have the same scale
 377 as sea level rise ($\sim 3\text{cm}$ per decade). By analyzing the positive and negative coherent eddy
 378 amplitude, we filter out the observed trends that come from a net increase in sea level.
 379 In fact, each coherent eddy polarity has intensified in the Southern Ocean and North East
 380 Pacific and Atlantic. In other words, the amplitude of each polarity has increased over
 381 time, and thus this strengthening is an intrinsic response of the coherent eddy field. Note
 382 that the negative coherent eddy amplitude dominates the global $|cEddy_{amp}|$ trends (Fig-
 383 ure 8e, f). However, different trend patterns can be observed in both positive and neg-
 384 ative coherent eddy amplitudes in the North Atlantic and North Pacific, where the neg-
 385 ative coherent eddy amplitude in the Western Boundary Currents appears to decrease.

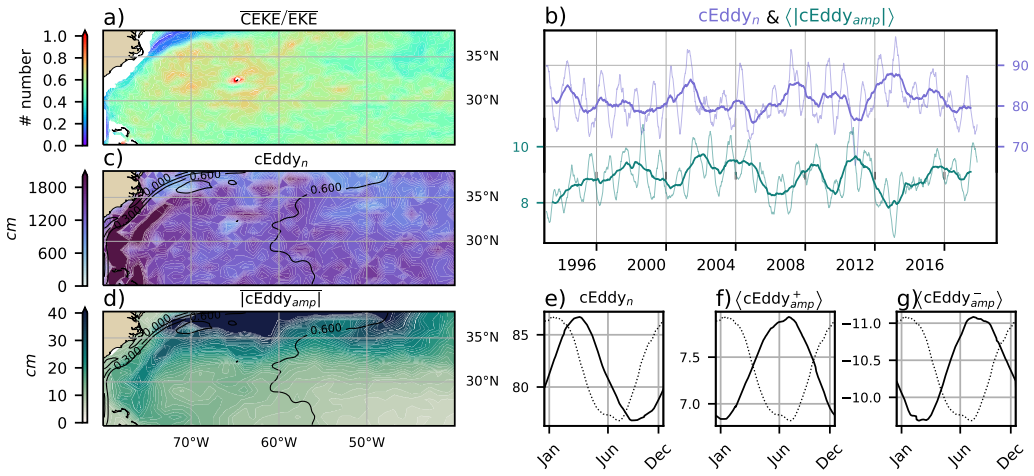
393 **6 Regional Climatology**

394 For regions with relatively large proportions of CEKE located at WBC extensions
 395 and eastern boundary currents, we investigate the seasonal and long-term variability of
 396 the coherent eddy properties. The most energetic WBC include the Gulf Stream, the Kuroshio
 397 Current, and the Agulhas Current (Figures 9, 10, and 11). Coherent eddy generation in
 398 boundary current extensions occurs through baroclinic and barotropic instabilities of the
 399 mean current, thus all these regions share similar generation dynamics. In all these re-
 400 gions without exception; (i) CEKE contains 50-80% of the EKE in regions equatorward
 401 from the mean WBC extensions, (ii) the number of eddies is consistently small over the
 402 mean WBC extensions, and (iii) the eddy amplitude is larger over the mean WBC ex-
 403 tensions.

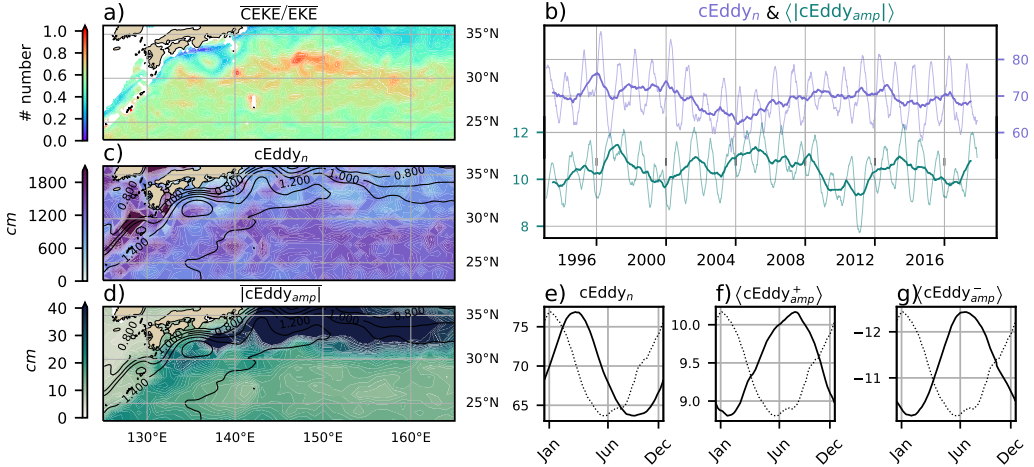
404 In the Gulf Stream, the energy ratio between CEKE and EKE is \sim 56% (Figure 9).
 405 The highest energy ratio occurs in regions with numerous eddies, colocated with regions
 406 where the largest $|cEddy_{amp}|$ gradients occur. The time series of $cEddy_n$ and $\langle |cEddy_{amp}| \rangle$
 407 are anti-correlated (-0.52), and they display interannual and seasonal variability. Although
 408 Chaudhuri et al. (2009) observed that a positive phase of the North Atlantic Oscillation
 409 (NAO) exhibits higher EKE, due to an increase in baroclinic instability, thus suggest-
 410 ing more coherent eddies, we do not find a correlation between the $cEddy_n$ or the $\langle |cEddy_{amp}| \rangle$
 411 in the Gulf Stream and the NAO index. Similar to the signal observed in the hemispheric
 412 analysis, the eddy count seasonal cycle follows the wind maximum lagging by \sim 3 months,
 413 while the amplitude of the coherent eddies lags by \sim 6 months.

422 The variability of the $cEddy_n$ and $\langle |cEddy_{amp}| \rangle$ in the Kuroshio Current are weakly
 423 anti-correlated (-0.41; Figure 10). However, on average 56% of the energy in the region
 424 corresponds to CEKE. As observed in the Gulf Stream, there is an important seasonal
 425 cycle in the boundary extension, where the eddy count seasonal cycle occurs in March,
 426 lagging the wind maximum by \sim 3 months (January). Meanwhile, the amplitude of the
 427 coherent eddies lags the wind maximum by \sim 6 months (June).

434 In the Southern Hemisphere the strongest boundary current, the Agulhas Current,
 435 shows similar behavior to its counterparts in the Northern Hemisphere (Figure 11). On
 436 average, coherent eddies in the Agulhas Current contain \sim 56% of the energy, meanwhile
 437 the $cEddy_n$ seasonal peak occurs in August, while the $\langle |cEddy_{amp}| \rangle$ peak occurs in January-
 438 February. The seasonal lag between the winds, eddy count, and eddy amplitude in each



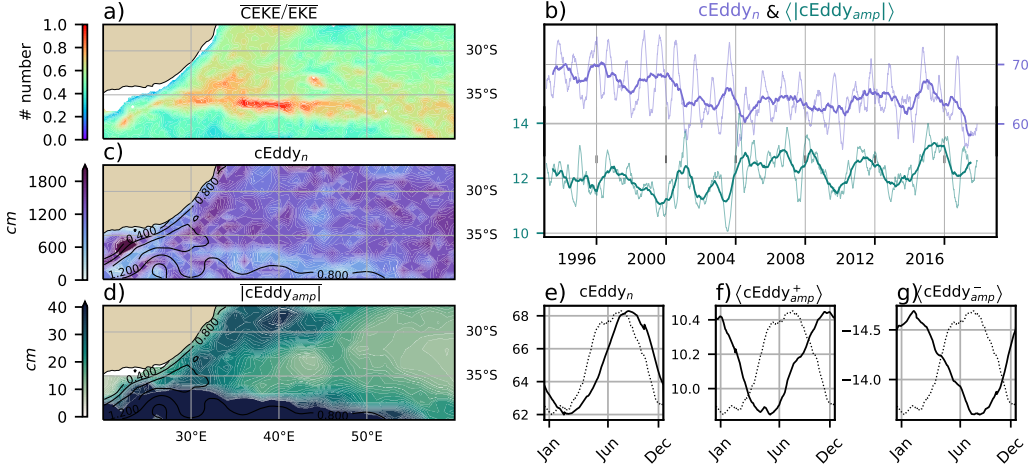
414 **Figure 9.** Climatology of the eddy field and coherent eddy field in the Gulf Stream. a) Ratio
 415 of mean coherent eddy kinetic energy (\overline{CEKE}) versus mean eddy kinetic energy (\overline{EKE}); b) Thick
 416 lines show the running average over 2 years and thin lines show the running average over 90 days
 417 of the coherent eddy number sum and the average coherent eddy amplitude; c) Map of the num-
 418 ber of eddies; d) Map of the average coherent eddy amplitude; e) Seasonal cycle of the number
 419 of eddies ($cEddy_n$); f) Seasonal cycle of the positive coherent eddy amplitude ($\langle cEddy_{amp}^+ \rangle$),
 420 and g) Seasonal cycle of the negative coherent eddy amplitude ($\langle cEddy_{amp}^- \rangle$). Contours in maps
 421 correspond to mean sea surface height (m).



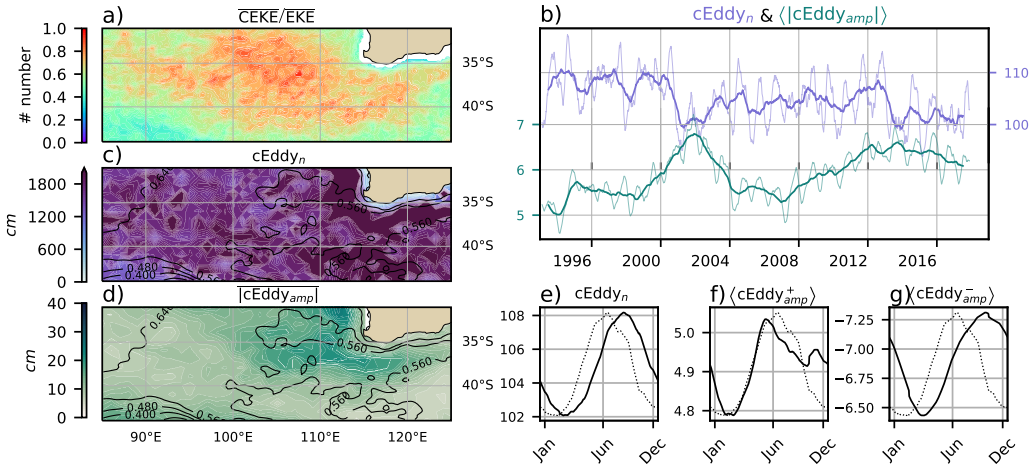
428 **Figure 10.** As in Figure 9, only showing the climatology of the eddy field and coherent eddy
 429 field in the Kuroshio extension. a) Ratio of mean coherent eddy kinetic energy ($\overline{\text{CEKE}}$) versus
 430 mean eddy kinetic energy ($\overline{\text{EKE}}$); b) Time-series of the coherent eddy number and the average
 431 coherent eddy amplitude; c) Map of the number of eddies; d) Map of the average coherent eddy
 432 amplitude; Seasonal cycle of the e) number of eddies; f) positive coherent eddy amplitude, and g)
 433 negative coherent eddy amplitude.

439 of the WBC extensions is interpreted as being analogous to the lagged response of co-
 440 herent eddy properties (Figure 6) due to eddy-eddy interactions, consistent with the in-
 441 verse cascade of energy.

448 Coherent eddies dominate the EKE field in other regions such as the Leeuwin Cur-
 449 rent (Figure 12), where 65% of the energy is contained by coherent eddies. The Leeuwin
 450 region is not characterized by having a large EKE, however, a considerable abundance
 451 of eddies and large eddy amplitudes are observed in the region. The time-series reveal
 452 a significant increase in the $\langle |c\text{Eddy}_{amp}| \rangle$, while the $c\text{Eddy}_n$ has decreased over the last
 453 3 decades. The seasonal cycle shows that the $c\text{Eddy}_n$ peak occurs in August, 3 months
 454 after the maximum winds (June). Meanwhile, the $\langle c\text{Eddy}_{amp}^+ \rangle$ responds in synchrony
 455 to the winds, and the $\langle c\text{Eddy}_{amp}^- \rangle$ is in phase with the seasonal cycle of the eddy num-
 456 ber ($c\text{Eddy}_n$). Hence, this region contrasts the behavior of WBC extensions, and show-
 457 cases the spatial variability of the seasonal cycle of coherent eddies.



442 **Figure 11.** As in Figure 9, only showing the climatology of the eddy field and coherent eddy
 443 field in the Agulhas Current. a) Ratio of mean coherent eddy kinetic energy ($\overline{\text{CEKE}}$) versus
 444 mean eddy kinetic energy ($\overline{\text{EKE}}$); b) Time-series of the coherent eddy number and the average
 445 coherent eddy amplitude; c) Map of the number of eddies; d) Map of the average coherent eddy
 446 amplitude; Seasonal cycle of the e) number of eddies; f) positive coherent eddy amplitude, and g)
 447 negative coherent eddy amplitude.



458 **Figure 12.** As in Figure 9, only showing the climatology of the eddy field and coherent eddy
 459 field in the Leeuwin Current. a) Ratio of mean coherent eddy kinetic energy ($\overline{\text{CEKE}}$) versus
 460 mean eddy kinetic energy ($\overline{\text{EKE}}$); b) Time-series of the coherent eddy number and the average
 461 coherent eddy amplitude; c) Map of the number of eddies; d) Map of the average coherent eddy
 462 amplitude; Seasonal cycle of the e) number of eddies; f) positive coherent eddy amplitude, and g)
 463 negative coherent eddy amplitude.

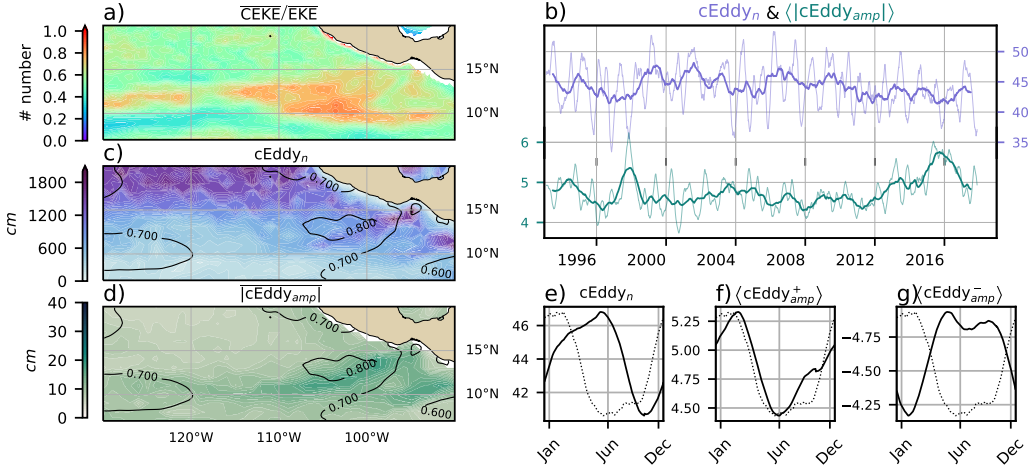


Figure 13. As in Figure 9, only showing the climatology of the eddy field and coherent eddy field in the East Tropical Pacific. a) Ratio of mean coherent eddy kinetic energy ($\overline{\text{CEKE}}$) versus mean eddy kinetic energy ($\overline{\text{EKE}}$); b) Time-series of the coherent eddy number and the average coherent eddy amplitude; c) Map of the number of eddies; d) Map of the average coherent eddy amplitude; Seasonal cycle of the e) number of eddies; f) positive coherent eddy amplitude, and g) negative coherent eddy amplitude.

Another region with important contributions to the coherent eddy field is the East Tropical Pacific (Tehuantepec region; Figure 13), where coherent eddies contain $\sim 58\%$ of the energy. In fact, coherent eddy generation in this region is modulated by winds and coastally trapped waves which produce a strong horizontal and vertical shear (baroclinic and barotropic instabilities; Zamudio et al., 2006). Furthermore, the equatorial generated waves propagating along the coast have an important interannual variability observable in the $\langle |c\text{Eddy}_{amp}| \rangle$ time-series, where El Niño events are notable during 1997 and 2015 (Figure 13b). The seasonal cycle of $c\text{Eddy}_n$, $\langle c\text{Eddy}_{amp}^+ \rangle$, and $\langle c\text{Eddy}_{amp}^- \rangle$ support the idea of a coherent eddy response to two different coherent eddy generation mechanisms; the number of eddies lags by ~ 3 months from the winds, while the $\langle c\text{Eddy}_{amp}^+ \rangle$ is in phase with the winds and the time of maximum trapped wave activity (winter; Zamudio et al., 2006), while the $\langle c\text{Eddy}_{amp}^- \rangle$ could be a consequence of eddy-eddy interactions.

483 **7 Discussion and Conclusions**

484 We have investigated the contribution of coherent eddies to the total kinetic en-
 485 ergy field using available satellite observations. We found that around half of the EKE
 486 is explained by coherent eddies. This half is concentrated in eddy-rich regions where a
 487 recent multi-decadal intensification of the eddy field has been observed (Martínez-Moreno
 488 et al., 2021). The energy contained by eddies is larger than the previous estimate of 40%
 489 by Chelton et al. (2011). Although there are differences in the identification criteria of
 490 both eddy identification methods, the main cause of the difference is likely to be the life-
 491 span and amplitude filters. These filters are widely used to track individual eddies in space
 492 and time, however, interactions between eddies in energetic regions may obscure the abun-
 493 dance and influence of short-lived coherent eddies. Filters are not used in this study, and
 494 indeed a lack of filters could facilitate an over-estimation of the the energy contained by
 495 coherent eddies, when mis-identifying or mis-fitting a coherent eddy.

496 It should also be noted that regions with first baroclinic Rossby radius of defor-
 497 mation smaller than 10km cannot be resolved by satellite observations. Thus, the en-
 498 ergy contained by coherent eddies around latitudes of 60° and those near the shore are
 499 missed from this estimate, and their role in the seasonal cycle and local dynamics remains
 500 unknown . New satellite altimeter missions (e.g. Surface Water and Ocean Topography;
 501 SWOT) may allow estimates of the energy contained by mesoscale coherent eddies out-
 502 side the subtropical regions and over the continental slope.

503 Hemisphere-wide variability indicates a strong seasonal cycle of the EKE, CEKE,
 504 and eddy properties. The seasonal cycle of the CEKE in each hemisphere occurs as a
 505 consequence of numerous small coherent eddies interacting with each other (eddy-eddy
 506 interactions) and resulting in stronger, larger and more energetic (but fewer) coherent
 507 eddies during summer, after a few months of the yearly coherent eddy number maxima.
 508 This result reveals eddy-eddy interactions and thus the transfer of energy from smaller
 509 coherent eddies to larger coherent eddies could explain the observed seasonal cycle of CEKE
 510 and coherent eddies properties.

511 Coherent eddy properties reveal a non-uniform long-term readjustment of the mesoscale
 512 eddy field. Overall, the eddy number has decreased globally at a significant rate of ∼35
 513 eddies per decade from ∼4000 eddies identified globally on average each day. Despite the
 514 small changes in the total eddy numbers, large proportions of the ocean show a major

strengthening of the mesoscale coherent eddy amplitude at rates greater than ~ 1 cm per decade. This strengthening of the coherent eddy amplitude is attributed to an intensification of each coherent eddy polarity, rather than a readjustment of the coherent eddy field to sea level rise. In other words, the coherent eddy amplitude intensification is occurring in both coherent eddy polarities and explains a proportion of the previously observed readjustments in the eddy field to long-term changes in the ocean forcing (Hu et al., 2020; Wunsch, 2020; Martínez-Moreno et al., 2021). This long-term readjustment reveals an intensification of the coherent eddy field, possibly due to long-term readjustments in the ocean baroclinic and barotropic instabilities, as well as the strength of the winds.

The reconstruction of the coherent eddies and their statistics has revealed regions with important coherent eddy contributions and a distinct seasonal evolution of the coherent eddies. Western boundary current (WBC) extensions generate eddies through the instability of the main currents and the seasonal cycle of coherent eddies, CEKE, and thus EKE could be associated with an inverse energy cascade observable through lagged seasonal cycles in the coherent eddy statistics. In addition, the amplitude of the seasonal cycle in WBC extensions is two times larger than any other region, thus the seasonality of the coherent eddies in WBC extensions dominates the hemispheric seasonal cycle. Furthermore, the seasonal lag of the inverse energy cascade is coupled with the presence of fronts (Qiu et al., 2014), such is the case for WBC extensions, and our results are consistent with the notion of baroclinic instability generating eddies and, via eddy-eddy interactions, a lagged inverse energy cascade.

The use of satellite observations in this study limits our ability to quantify the importance of the inverse energy cascade seasonality in the control of the coherent eddy seasonal cycle. As mentioned above, there is robust evidence of an increase in eddy-eddy interactions, however we cannot discard important contributions from other processes such as the seasonal cycle of forcing, stratification, and instabilities, which are crucial in the generation of coherent eddies. Although this study can provide a descriptive response of the coherent eddy field, further work is needed to assess the role of eddy-eddy interactions in our changing climate, ocean dynamics, and biogeochemical processes. Furthermore, the SWOT mission could allow us to advance our understanding of eddy-eddy interactions and the seasonal cycle of scales smaller than mesoscale, which may provide further evidence of the inverse energy cascade driving the coherent eddy seasonality. **Cur-**

548 rent generation climate models have just started to resolve mesoscale dynam-
 549 ics, thus, the presented estimate of energy in coherent eddies from satellite
 550 observations could be used as a benchmark that facilitates the evaluation of
 551 such models, and to quantify the energy contained by mesoscale and more
 552 specifically coherent eddies in future climate projections.

553 **Acknowledgments**

554 The Chelton & Schlaak (2013) dataset was produced by SSALTO/DUACS and distributed
 555 by AVISO+ (<https://www.aviso.altimetry.fr/>) with support from CNES, developed
 556 and validated in collaboration with E.Mason at IMEDEA. Global coherent eddy recon-
 557 struction, coherent and non-coherent eddy kinetic energy datasets, in addition to grid-
 558 ded coherent eddy tracking datasets are publicly available at (<https://doi.org/10.5281/zenodo.4646429>). All analyses and figures in this manuscript are reproducible via Jupyter
 559 notebooks and instructions can be found in the Github repository `CEKE_climatology`
 560 (https://github.com/josuemtzmo/CEKE_climatology). Trends used the Python Pack-
 561 age `xarrayMannKendall` (<https://doi.org/10.5281/zenodo.4458776>). J.M.-M. was
 562 supported by the Consejo Nacional de Ciencia y Tecnología (CONACYT), Mexico fund-
 563 ing. M.H.E. is supported by the Centre for Southern Hemisphere Oceans Research (CSHOR),
 564 a joint research centre between Qingdao National Laboratory for Marine Science and Tech-
 565 nology (QNLM), Commonwealth Scientific and Industrial Research Organisation (CSIRO),
 566 University of New South Wales (UNSW), and the University of Tasmania (UTAS). Anal-
 567 yses were undertaken on the National Computational Infrastructure in Canberra, Aus-
 568 tralia, which is supported by the Australian Commonwealth Government.

570 **References**

- 571 Arbic, B. K., Polzin, K. L., Scott, R. B., Richman, J. G., & Shriver, J. F. (2013).
 572 On Eddy Viscosity, Energy Cascades, and the Horizontal Resolution of Gridded
 573 Satellite Altimeter Products*. *Journal of Physical Oceanography*, 43(2), 283–300.
 574 doi: 10.1175/jpo-d-11-0240.1
- 575 Ashkezari, M. D., Hill, C. N., Follett, C. N., Forget, G., & Follows, M. J. (2016).
 576 Oceanic eddy detection and lifetime forecast using machine learning methods.
 577 *Geophysical Research Letters*, 43(23). doi: 10.1002/2016gl071269
- 578 Beron-Vera, F. J., Wang, Y., Olascoaga, M. J., Goni, G. J., & Haller, G. (2013). Ob-

- 579jective Detection of Oceanic Eddies and the Agulhas Leakage. *Journal of Physical*
580*Oceanography*, 43(7), 1426–1438. doi: 10.1175/JPO-D-12-0171.1
- 581Bouali, M., Sato, O. T., & Polito, P. S. (2017). Temporal trends in sea surface tem-
582perature gradients in the South Atlantic Ocean. *Remote Sensing of Environment*,
583194, 100–114. doi: 10.1016/j.rse.2017.03.008
- 584Callies, J., Flierl, G., Ferrari, R., & Fox-Kemper, B. (2015). The role of mixed-layer
585instabilities in submesoscale turbulence. *Journal of Fluid Mechanics*, 788, 5–41.
586doi: 10.1017/jfm.2015.700
- 587Cane, M. A., Clement, A. C., Kaplan, A., Kushnir, Y., Pozdnyakov, D., Seager, R.,
588... Murtugudde, R. (1997). Twentieth-Century Sea Surface Temperature Trends.
589*Science*, 275(5302), 957–960. doi: 10.1126/science.275.5302.957
- 590Chaudhuri, A. H., Gangopadhyay, A., & Bisagni, J. J. (2009). Interannual variabil-
591ity of Gulf Stream warm-core rings in response to the North Atlantic Oscillation.
592*Continental Shelf Research*, 29(7), 856–869. doi: 10.1016/j.csr.2009.01.008
- 593Chelton, D. B., A. d. R., Schlax, M. G., Naggar, K., & Siwetz, N. (1998). Geo-
594graphical variability of the first baroclinic Rossby radius of deformation. *Journal*
595*of Physical Oceanography*, 28(3), 433–460. doi: 10.1175/1520-0485(1998)028<433:
596GVOTFB>2.0.CO;2
- 597Chelton, D. B., Gaube, P., Schlax, M. G., Early, J. J., & Samelson, R. M. (2011).
598The influence of nonlinear mesoscale eddies on near-surface oceanic chlorophyll.
599*Science*, 334(6054), 328–32. doi: 10.1126/science.1208897
- 600Chelton, D. B., & Schlax, M. G. (2013). *Mesoscale eddies in altimeter observations*
601*of ssh*.
- 602Chelton, D. B., Schlax, M. G., Samelson, R. M., & de Szoeke, R. A. (2007). Global
603observations of large oceanic eddies. *Geophysical Research Letters*, 34(15),
604L15606. doi: 10.1029/2007GL030812
- 605CMEMS. (2017). The Ssalto/Duacs altimeter products were produced and dis-
606tributed by the Copernicus Marine and Environment Monitoring Service. *Aviso*
607*Dataset*. Retrieved from <https://www.aviso.altimetry.fr/>
- 608Cui, W., Wang, W., Zhang, J., & Yang, J. (2020). Identification and census statis-
609tics of multicore eddies based on sea surface height data in global oceans. *Acta*
610*Oceanologica Sinica*, 39(1), 41–51. doi: 10.1007/s13131-019-1519-y
- 611Faghmous, J. H., Frenger, I., Yao, Y., Warmka, R., Lindell, A., & Kumar, V. (2015,

- 612 6). A daily global mesoscale ocean eddy dataset from satellite altimetry. *Scientific*
613 *Data*, 2, 150028 EP -. doi: 10.1038/sdata.2015.28
- 614 Ferrari, R., & Wunsch, C. (2009). Ocean Circulation Kinetic Energy: Reservoirs,
615 Sources, and Sinks. *Annual Review of Fluid Mechanics*, 41(1), 253–282. doi: 10
616 .1146/annurev.fluid.40.111406.102139
- 617 Frenger, I., Gruber, N., Knutti, R., & Münnich, M. (2013). Imprint of Southern
618 Ocean eddies on winds, clouds and rainfall. *Nature Geoscience*, 6(8), 608 EP -.
619 doi: 10.1038/ngeo1863
- 620 Frenger, I., Münnich, M., Gruber, N., & Knutti, R. (2015). Southern Ocean eddy
621 phenomenology. *Journal of Geophysical Research: Oceans*, 120(11), 7413-7449.
622 doi: 10.1002/2015JC011047
- 623 Fu, L., Chelton, D., Le Traon, P., & Oceanography, M. R. (2010). Eddy dynamics
624 from satellite altimetry. *Oceanography*, 23(4), 14-25. doi: 10.2307/24860859
- 625 Gill, A., Green, J., & Simmons, A. (1974). Energy partition in the large-scale ocean
626 circulation and the production of mid-ocean eddies. *Deep Sea Res Oceanogr Abstr*,
627 21(7), 499-528. doi: 10.1016/0011-7471(74)90010-2
- 628 Hogg, A. M., & Blundell, J. R. (2006). Interdecadal variability of the southern
629 ocean. *Journal of Physical Oceanography*, 36(8), 1626-1645. doi: 10.1175/
630 JPO2934.1
- 631 Hogg, A. M., Meredith, M. P., Chambers, D. P., Abrahamsen, E. P., Hughes,
632 C. W., & Morrison, A. K. (2015). Recent trends in the Southern Ocean
633 eddy field. *Journal of Geophysical Research: Oceans*, 120(1), 257-267. doi:
634 10.1002/2014JC010470
- 635 Hu, S., Sprintall, J., Guan, C., McPhaden, M. J., Wang, F., Hu, D., & Cai,
636 W. (2020, 2). Deep-reaching acceleration of global mean ocean circula-
637 tion over the past two decades. *Science Advances*, 6(6), eaax7727. doi:
638 10.1126/sciadv.aax7727
- 639 Japan Meteorological Agency, Japan. (2013). *Jra-55: Japanese 55-year reanalysis*,
640 *daily 3-hourly and 6-hourly data*. Boulder CO: Research Data Archive at the Na-
641 tional Center for Atmospheric Research, Computational and Information Systems
642 Laboratory. Retrieved from <https://doi.org/10.5065/D6HH6H41>
- 643 Kang, D., & Curchitser, E. N. (2013). Gulf stream eddy characteristics in a high-
644 resolution ocean model. *Journal of Geophysical Research: Oceans*, 118(9), 4474-

- 645 4487. Retrieved from <https://agupubs.onlinelibrary.wiley.com/doi/abs/10.1002/jgrc.20318> doi: <https://doi.org/10.1002/jgrc.20318>
- 646 Kang, D., & Curchitser, E. N. (2017). On the Evaluation of Seasonal Variability of
647 the Ocean Kinetic Energy. *Geophysical Research Letters*, 47, 1675-1583. doi: 10
648 .1175/JPO-D-17-0063.1
- 649 Li, G., Cheng, L., Zhu, J., Trenberth, K. E., Mann, M. E., & Abraham, J. P. (2020).
650 Increasing ocean stratification over the past half-century. *Nature Climate Change*,
651 1–8. doi: 10.1038/s41558-020-00918-2
- 652 Martínez-Moreno, J., Hogg, A. M., England, M., Constantinou, N. C., Kiss, A. E.,
653 & Morrison, A. K. (2021). Global changes in oceanic mesoscale currents over the
654 satellite altimetry record. *Journal of Advances in Modeling Earth Systems*, 0(ja).
655 doi: 10.1029/2019MS001769
- 656 Martínez-Moreno, J., Hogg, A. M., Kiss, A. E., Constantinou, N. C., & Morrison,
657 A. K. (2019). Kinetic energy of eddy-like features from sea surface altimeter.
658 *Journal of Advances in Modeling Earth Systems*, 11(10), 3090-3105. doi:
659 10.1029/2019MS001769
- 660 Patel, R. S., Llort, J., Strutton, P. G., Phillips, H. E., Moreau, S., Pardo, P. C.,
661 & Lenton, A. (2020). The Biogeochemical Structure of Southern Ocean
662 Mesoscale Eddies. *Journal of Geophysical Research: Oceans*, 125(8). doi:
663 10.1029/2020jc016115
- 664 Pilo, G. S., Mata, M. M., & Azevedo, J. L. L. (2015). Eddy surface properties and
665 propagation at Southern Hemisphere western boundary current systems. *Ocean
666 Science*, 11(4), 629–641. doi: 10.5194/os-11-629-2015
- 667 Qiu, B. (1999). Seasonal Eddy Field Modulation of the North Pacific Subtropical
668 Countercurrent: TOPEX/Poseidon Observations and Theory. *Journal of Physical
669 Oceanography*, 29(10), 2471–2486. doi: 10.1175/1520-0485(1999)029<2471:sefmot>2
670 .0.co;2
- 671 Qiu, B., & Chen, S. (2004). Seasonal Modulations in the Eddy Field of the South
672 Pacific Ocean. *Journal of Physical Oceanography*, 34(7), 1515–1527. doi: 10.1175/
673 1520-0485(2004)034<1515:smitef>2.0.co;2
- 674 Qiu, B., Chen, S., Klein, P., Sasaki, H., & Sasai, Y. (2014). Seasonal Mesoscale
675 and Submesoscale Eddy Variability along the North Pacific Subtropical Coun-
676 tercurrent. *Journal of Physical Oceanography*, 44(12), 3079–3098. doi:
677

- 678 10.1175/JPO-D-14-0071.1
- 679 Ruela, R., Sousa, M. C., deCastro, M., & Dias, J. M. (2020). Global and regional
680 evolution of sea surface temperature under climate change. *Global and Planetary
681 Change*, 190, 103190. doi: 10.1016/j.gloplacha.2020.103190
- 682 Sasaki, H., Klein, P., Qiu, B., & Sasai, Y. (2014). Impact of oceanic-scale inter-
683 actions on the seasonal modulation of ocean dynamics by the atmosphere. *Nature
684 Communications*, 5(1), 5636. doi: 10.1038/ncomms6636
- 685 Schubert, R., Schwarzkopf, F. U., Baschek, B., & Biastoch, A. (2019). Submesoscale
686 Impacts on Mesoscale Agulhas Dynamics. *Journal of Advances in Modeling Earth
687 Systems*, 11(8), 2745–2767. doi: 10.1029/2019ms001724
- 688 Siegel, D., Peterson, P., DJ, M., Maritorena, S., & Nelson, N. (2011). Bio-optical
689 footprints created by mesoscale eddies in the Sargasso Sea. *Geophysical Research
690 Letters*, 38(13), n/a-n/a. doi: 10.1029/2011GL047660
- 691 Uchida, T., Abernathey, R., & Smith, S. (2017). Seasonality of eddy kinetic energy
692 in an eddy permitting global climate model. *Ocean Modelling*, 118, 41-58. doi: 10
693 .1016/j.ocemod.2017.08.006
- 694 Wunsch, C. (2020). Is The Ocean Speeding Up? Ocean Surface Energy Trends.
695 *Journal of Physical Oceanography*, 50(11), 1–45. doi: 10.1175/jpo-d-20-0082.1
- 696 Wunsch, C., & Ferrari, R. (2004). Vertical mixing, energy, and the general circula-
697 tion of the oceans. *Annual Review of Fluid Mechanics*, 36(1), 281–314. doi: 10
698 .1146/annurev.fluid.36.050802.122121
- 699 Wyrtki, K., Magaard, L., & Hager, J. (1976). Eddy energy in the oceans. *Journal of
700 Geophysical Research*, 81(15), 2641-2646. doi: 10.1029/JC081i015p02641
- 701 Yue, S., & Wang, C. (2004). The Mann-Kendall Test Modified by Effective Sample
702 Size to Detect Trend in Serially Correlated Hydrological Series. *Water Resources
703 Management*, 18(3), 201–218. doi: 10.1023/b:warm.0000043140.61082.60
- 704 Zamudio, L., Hurlbert, H. E., Metzger, E. J., Morey, S. L., O'Brien, J. J., Tilburg,
705 C., & Zavala-Hidalgo, J. (2006). Interannual variability of Tehuantepec ed-
706 dies. *Journal of Geophysical Research: Oceans (1978–2012)*, 111(C5). doi:
707 10.1029/2005JC003182